Visible-light photocatalytic degradation of dyes by TiO2 -Au inverse opal films synthesized by Atomic Layer Deposition

P. Birnal, M. C. Marco de Lucas, I. Pochard, F. Herbst, O. Heintz, L. Saviot, B. Domenichini, L. Imhoff

Visible-light photocatalytic degradation of dyes by TiO_2–Au inverse opal films synthesized by Atomic Layer Deposition

P. Birnal[a,c,1,*], M. C. Marco de Lucas [a,2,*], I. Pochard[b,3], F. Herbst[a,4], O. Heintz[a,5], L. Saviot[a,6], B. Domenichini[a,7], L. Imhoff[a,8]

[a] *Laboratoire Interdisciplinaire Carnot de Bourgogne (ICB), UMR 6303 CNRS-Université Bourgogne-Franche Comté, 9 Av. A. Savary, BP 47 870, 21078 Dijon Cedex, France*
[b] *Institut Univers, Temps-fréquence, Interfaces, Nanostructures, Atmosphère et environnement, Molécules (UTINAM), UMR 6213 CNRS-Université Bourgogne-Franche Comté, 41 bis avenue de l'Observatoire, 25010 Besançon Cedex, France*
[c] *Interfaces, Confinement, Matériaux et Nanostructures (ICMN) UMR7374 CNRS - Université d'Orléans,1B rue de la Férollerie, CS 40059, 45071 ORLEANS CEDEX 2, France*

Abstract

TiO_2–Au composite planar films and inverse opals were synthesized by Atomic Layer Deposition (ALD) using Direct Liquid Injection for TiO_2 deposition and for the injection of preformed Au nanoparticles (NPs). A few nanometers thick layer of TiO_2 was deposited after the Au NPs. Thermal annealing at 380°C allowed to remove the polystyrene beads template and to form anatase TiO_2.

The obtained inverse opals have a layered structure of hollow TiO_2 spheres interconnected by channels formed at the template beads contacts. Au NPs are homogeneously distributed on the surface. Their localized surface plasmon resonance (SPR) at 587 nm confirm that they are embedded in TiO_2. These photocatalysts were tested for the degradation of methylene blue solutions under visible-light illumination. A significant photocatalytic effect is reported with a 95% degradation after 7 h of exposure only for the composite inverse opal. This results from the transfer of hot electrons from the NPs excited at their SPR to the conduction band of TiO_2. They generate reactive oxygen species at the surface of TiO_2 which are involved in the initial stage of MB degradation. These results highlight the potential of ALD for the fabrication of complex composite structures for application in photocatalysis.

*Corresponding authors
Email addresses: pierre.birnal@cnrs-orleans.fr (P. Birnal), delucas@u-bourgogne.fr (M. C. Marco de Lucas)
[1]ORCID: 0000-0003-0486-9953
[2]ORCID: 0000-0001-5135-4026
[3]ORCID: 0000-0001-7938-960X
[4]ORCID: 0000-0002-7774-4433
[5]ORCID: 0000-0001-5512-4973
[6]ORCID: 0000-0002-1249-2730
[7]ORCID: 0000-0002-2567-3610
[8]ORCID: 0000-0003-1115-5342

Keywords: inverses opals, photocatalysis, Atomic Layer Deposition, nanocomposites

1. Introduction

Wastewater pollution is a major environmental issue. Dyes used in the textile and pharmaceutical industries are an important part of this pollution. Approximately 15% of the total world production of dyes is discharged in wastewater [1]. These pollutants are generally considered to be toxic for animals and plants. Most of them are poorly biodegradable or resistant to environmental conditions [2]. This is why important research efforts are currently being made on photocatalysis and adsorption methods to degrade or eliminate these products [3–8].

Titanium dioxide (TiO_2) is the one of the most studied photocatalysts [6, 9, 10]. It is widely used in industry [11–13] because it is non toxic to humans, chemically stable and low cost. However, its photocatalytic activity is hindered by charge photocarriers recombination [14, 15]. Moreover, the absorption of TiO_2 is mostly restricted to UV wavelengths which correspond to a small part of the solar spectrum. Different methods have been proposed to improve the photo-electronic properties of TiO_2 in order to overcome these drawbacks and enhance the activity of TiO_2-based photocatalysts. Nanostructured titanium dioxide and nanocomposites coupling TiO_2 with different types of materials (graphene, carbon nanotubes, quantum dots, ...) have been widely developed and tested as photocatalysts for wastewater treatment [8, 16–20].

Coupling TiO_2 with plasmonic nanostructures is one of the ways explored to extend the photocatalytic window to visible light. Several mechanisms have been proposed to explain the higher activity of plasmonic photocatalysts under visible light illumination that matches their localized surface plasmon resonance (LSPR). Linic *et al.* have described three main and non-mutually exclusive mechanisms: direct charge injection, near-field enhancement, and extended optical path length by plasmon induced scattering [21]. The latter one can be neglected in the case of small plasmonic nanoparticles whose diameter is small compared to the wavelength of light. The enhanced near-field mechanism is based on the hypothesis of a radiative energy transfer between the plasmonic nanoparticle and the semiconductor under illumination at the surface plasmon resonance wavelength. This effect can be neglected in the case of TiO_2 which has no photocatalytic activity in the visible range.

The direct charge injection mechanism is based on the transfer of energetic electrons (*hot* electrons) from the nanoparticle excited at the plasmon resonance to the conduction band of TiO_2. Hot electron transfer requires intimate electrochemical contact between the plasmonic particle and the semiconductor. Zheng *et al.* have recently reported a study of the dynamics of the hot electrons transfer using the photocatalytic reduction of p-nitrothiophenol as model reaction [22]. The influence of the Au NPs size on the hot electrons transfer was investigated by operando Surface Enhanced Raman Spectroscopy (SERS). It was concluded that the LSPR intensity and the electron diffusion efficiency at the space charge layer around the metal-semiconductor junction is intrinsically related to the size of the metal nanoparticles. The direct charge injection mechanism has been widely proposed in the literature to explain the higher photoactivity of TiO_2 nanostructures doped with noble metal nanoparticles. Recent works have

studied the influence of the size of the nanoparticles used, as well as the nanoparticle loading, on the activity of TiO_2–Au photocatalysts [23, 24].

In parallel to the methods aiming at improving the photo-electronic properties of TiO_2, different kinds of TiO_2 nanostructures with a large specific surface have been developed to increase the activity of TiO_2 based photocatalysts. The synthesis of photonic crystal photocatalysts such as opals and inverse opals (IO) structures corresponds to this approach, but in addition it benefits from specific optical properties due to the photonic band gap of these structures [25]. The decrease of the velocity of light propagation at the edge of the photonic band ("slow light" effect) induces reflections in the material that can enhance its optical absorption. The synergy of the photonic crystal properties and the high specific surface offers a great potential for photonic crystals structures in photocatalysis [26–28].

Recently, several works have reported the synthesis of TiO_2 IO decorated with noble-metal nanoparticles for photocatalysis applications under visible light illumination [29–32]. The synthesis of this type of structures has been developed by sol-gel methods, electrochemical deposition, chemical vapor deposition and atomic layer deposition by using self-assembled templates of polymer beads, followed by calcination to remove the template [26, 33]. Among these techniques, the ALD approach offers an excellent control of the synthesized film at the expense of a lower growth rate than the classical Chemical Vapor Deposition (CVD) process. Moreover, ALD is used to fabricate films with a very good conformity on complex shape substrates because the gas flow bringing the precursors covers all the available surfaces. This results in a homogeneous layer on the substrate with a perfectly controlled thickness. In addition, the ALD technique can operate at lower temperature than the CVD process, which allows the use of substrates that degrade at relatively low temperatures, such as polymers.

The goal of the present work was to synthesize TiO_2–Au composite inverse opals by Atomic Layer Deposition (ALD) using a Direct Liquid Injection (DLI) setup not only for TiO_2 deposition but also for the injection of preformed Au-NPs. In addition, this method allows to coat the deposited nanoparticles with a thin layer of TiO_2 to improve their adhesion on the TiO_2 surface. The structure and composition of the synthesized composite inverse opals and planar films were analyzed by Raman spectroscopy, Secondary Ions Mass Spectroscopy (SIMS) and X-ray Photoelectrons Spectroscopy (XPS). The degradation of methylene blue (MB) solutions was studied to assess the photocatalytic activity of the synthesized composite structures under visible-light. The study was done under natural pH of the MB solution. Therefore, only the specific surface area and the presence or not of Au NPs vary and are responsible for the differences in photocatalytic efficiency from one sample to another.

2. Experimental details

2.1. Fabrication of TiO_2–Au films

All the samples were fabricated using a Direct Liquid Injection Metal-Organic Chemical Vapor Deposition (DLI-MOCVD) process with rapid thermal heating (Annealsys MC-050). The DLI setup is based on atomized liquid injection of the precursor solution to generate the reactive vapor. This device works in CVD or ALD mode depending on to the operating parameters [34, 35].

Silicon (100) substrates were cleaned by successive solvent baths (cyclohexane, acetone and ethanol) and laid on a silicon carbide coated graphite susceptor supported by a quartz holder inside a quartz reactor. The working pressure in the reaction chamber was kept below 20 mbar using a dry pump and a regulator valve. The temperature of the susceptor near the sample was measured by a K-type thermocouple and maintained at 90 °C during deposition.

The precursors used to fabricate TiO_2 film by ALD were tetrakis(dimethylamido)-titanium(IV) (TDMAT, Sigma Aldrich, 99.999%) and deionized water. The TDMAT solution was diluted in cyclohexane (C_6H_{12}, 99.99%, Sigma Aldrich) at a concentration of 0.02 M. The titanium precursor was kept at room temperature and pressurized in a vessel under 3 bars of 99.999% pure nitrogen used as carried gas. The deionized water was kept in a tank under vacuum to get a saturated vapor atmosphere to be injected into the reaction chamber. TiO_2 thin films were fabricated using the deposition conditions reported in [33] (precursors injection and purges times).

The deposition of gold nanoparticles was done at room temperature by liquid injection of a diluted suspension of commercial Au-NPs into the reaction chamber using the DLI device. The suspension of citrate-stabilized gold-nanoparticles in water was provided by Sigma-Merk. The diameter of the gold NPs was 5 nm and the surface plasmon resonance of the solution was at about 520 nm. The concentration of nanoparticles was about 5.5×10^{13} particles/mL. Several solvents were checked to dilute this commercial suspension before the injection into the reaction chamber. Ethanol provided the best results in terms of NPs dispersion and low impact on the ALD growth of a thin film of TiO_2 covering the first layer of TiO_2 decorated with gold NPs. A 10-fold dilution was carried out and stocked in a flask connected to the deposition set-up by an injector. The suspension was pressurized with nitrogen under a pressure of 1 bar and injection pulses were set with an injection duration of 5 ms and a frequency of 0.5 Hz for 80 minutes.

Inverse opals films were synthesized using a template of polystyrene (PS) beads of 500 nm in diameter (from Alfa Aesar with a 2.5 wt% suspension of PS beads in water). The beads were spin-coated on a silicon substrate (acceleration 100 tr/mn/s, steady speed 1500 tr/mn, duration 60 s). The obtained monolayers of beads has an hexagonal compact structure. A 40 nm thick layer of TiO_2 was synthesized by ALD on the template with the same parameters as for the TiO_2 planar coatings. For the composite films, Au NPs were injected at room temperature using the same parameters as for the planar films. Then, a 5 nm thick layer of TiO_2 was deposited by ALD on top of the samples to protect them from the external environment and to increase the contact surface area between gold and TiO_2. Finally, the samples were annealed in the reaction chamber at 380 °C for 3 hours to eliminate the polystyrene template and induce the crystallization of TiO_2. Inverse opal films formed of interconnected shells were obtained in this way.

Four kinds of samples were synthesized on Si substrates (Figure 1):

(a) **P–TiO_2**: Planar 100 nm thick films of pure TiO_2;
(b) **P–TiO_2–Au**: Planar composite TiO_2–Au films composed of a 95 nm thick ALD layer of TiO_2 on which Au NPS were deposited. A 5 nm thick film of TiO_2 layer was deposited on top of the sample;
(c) **IO–TiO_2**: inverse opals of pure TiO_2;

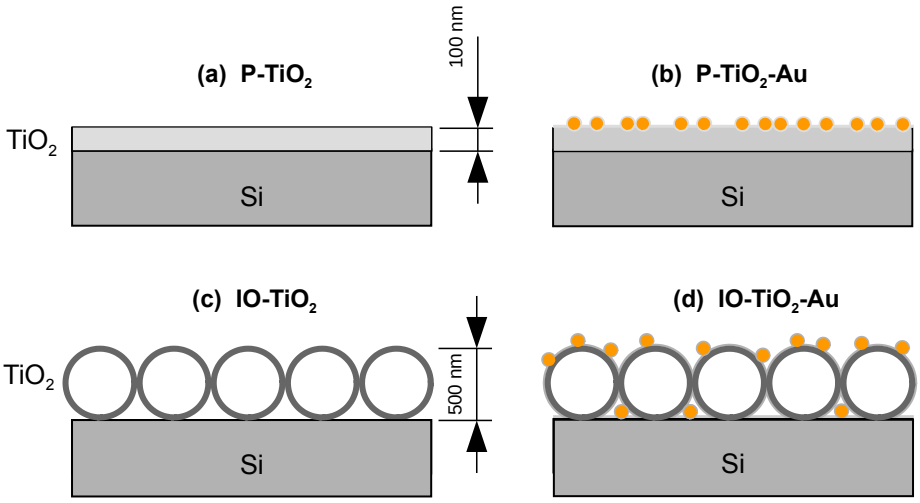

Figure 1: Schematic representation of the different structures synthesized in this work: (a) planar TiO_2 film, (b) planar TiO_2 film decorated with Au-NPs on the top, (c) inverse opal TiO_2 film, and (d) inverse opal TiO_2 film decorated with Au-NPs.

(d) **IO–TiO_2–Au**: composite TiO_2–Au inverse opals.

The planar films were also annealed in the reaction chamber under a pressure of 10 mbar at 380 °C for 3 hours.

2.2. Characterization methods and photocatalysis experiments

The surface and cross-section morphology of the samples were observed by scanning electron microscopy (SEM) using a JEOL 7600F working between 1 and 3 kV. The backscattered electrons mode was used to visualize the distribution of gold nanoparticles on the TiO_2 surface whereas the secondary electron mode was used to get a precise morphology of the films.

Characterizations of the chemical composition of TiO_2 films were performed by X-ray photoelectron spectroscopy (XPS) using a XPS-Auger PHI 5000 Versaprobe with monochromatized Al Kα as the X-ray source at 1486.6 eV.

Complementary nano-SIMS analyses were carried out to confirm the SEM observations and to obtain the depth-profile of the Au NPs. The measurements were performed using a PHI nanoTOF II working with Bi_3^{2+} ions (30 keV). Due to the presence of gold, a Cs^+ ion beam (2 keV) was chosen to sputter the sample surface. The analyzed area is a square of 40 μm^2, whereas the sputtered surface is a square of 400 μm^2, both of them being carried out in raster mode. The elementary composition of the film is obtained as a function of the sputtering time.

Raman spectroscopy was used to investigate the structural properties of the films. The measurements were performed at room temperature using a Renishaw inVia micro-Raman spectrometer in backscattering configuration. The spectra were recorded with a

532 nm laser as the excitation source and a $\times 100$ microscope objective (NA=0.9). The laser power was about 0.5 mW to avoid heating the samples.

The photocatalytic activity for the degradation of dyes by the different films was tested with an aqueous solution of methylene blue (MB) concentrated at 1 μmol/L. The MB solution was placed in a cuvette ($1 \times 1 \times 4.5$ cm^3) with a sample of the selected catalyst (1 cm^2). The system was stirred for 10 minutes every hour by ultrasounds and irradiated by a lamp at a distance of 1 cm. A Philips Tornado lamp with a color temperature of 6500 K was used as illumination source. The irradiance was about 100 mW/cm^2 at 1 cm from the lamp. The absorption spectrum of the MB solution was recorded with a Shimadzu UV-2550 spectrometer at regular time intervals.

3. Results and discussion

3.1. Morphological and structural characterizations

The morphology of the planar films and inverse opals was imaged by SEM in the backscattered electrons mode to take advantage of the chemical contrast between the TiO_2 films and the deposited Au NPs.

Figure 2a shows the surface of a P–TiO_2–Au planar film deposited on a Si substrate where the homogeneous distribution of Au NPs and a few agglomerated nanoparticles can be seen. Annealing 3 hours at 380 °C did not affect the nanoparticles distribution on the surface. The cross-section view (Fig. 2b) shows the homogeneous and compact TiO_2 layer grown by ALD on the Si substrate. As expected, the Si–TiO_2 interface is barely visible. There is no delamination of the film or voids at the film–substrate interface. Au NPs are seen on the top of the sample. They are at least partially embedded in the very thin top TiO_2 layer.

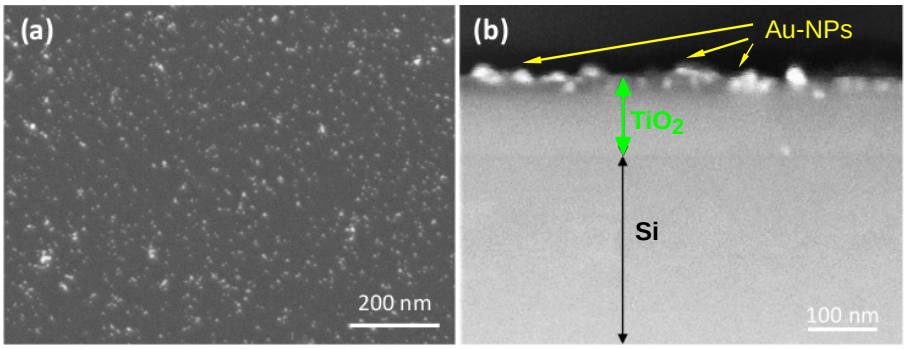

Figure 2: SEM surface (a) and cross-section (b) of P–TiO_2–Au deposited on a Si substrate and post-annealed at 380 °C during 3h. These images were obtained with the backscattered electrons mode.

The surface views of IO–TiO_2–Au inverse opals are given in Figures 3a and 3b. They show the ordered arrangement of spheres made of TiO_2 which corresponds to the opal structure of the template. The images also show a fairly homogeneous distribution of nanoparticles on the surface of the TiO_2 shells even after annealing, a slightly higher density near the contact points between the spheres, and few agglomerated NPs.

The calcination efficiency of the PS beads that made up the template was checked by ion beam etching during 2 minutes of the top of the spheres. As seen in Figures 3c and 3d, the PS beads have completely disappeared and hollow TiO_2 shells remain which are interconnected by channels corresponding to the contact points between the PS beads in the template as shown in Figure 3d. The presence of Au NPs at the surface of these shells is clearly observed.

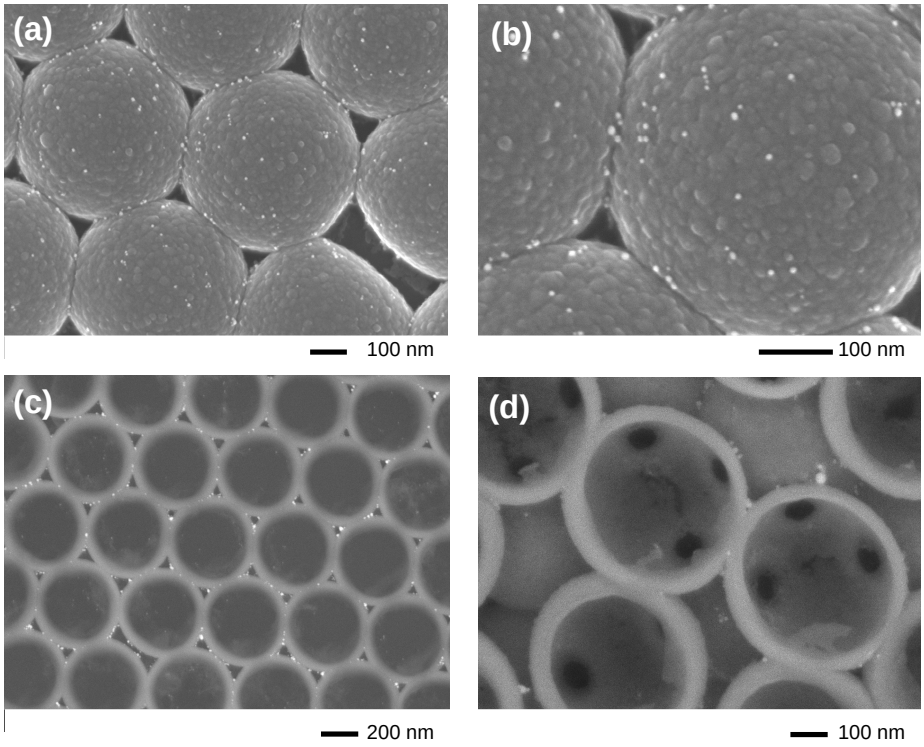

Figure 3: Backscattered electrons SEM images of IO–TiO_2–Au. The thickness of TiO_2 is 45 nm. Gold nanoparticles were deposited on the surface. The sample was annealed 3h at 380 °C. (a,b) Surface and (c,d) interior images of the hollow shells obtained after partial ionic etching of the upper shells layer.

The in-depth distribution of Au NPs in P–TiO_2–Au and IO–TiO_2–Au samples was studied by nano-SIMS. Figure 4 shows the intensity as a function of the sputtering time measured for the peaks corresponding to the Si^+ (28.01 u.m.a.), TiO_2^+ (79.9 u.m.a.) and Au^- (197.0 u.m.a.) ions.

For the P–TiO_2–Au planar film, Figure 4a shows for Si^+ a step profile centered at about 100 s. On the contrary, the intensity of TiO_2^+ decreases with the sputtering, and it decreases faster after 100 s. This result together with the variation observed for the Si^+ peak indicate that the film-substrate interface is reached for a sputtering time of about 100 s. The signal of Au^- shows a narrow peak centered in the first 10 s of sputtering, which can be assigned to gold nanoparticles deposited on TiO_2. It is difficult to draw any conclusion regarding the presence of the few nanometers thick

TiO_2 film deposited on top of the gold nanoparticles. The UV-vis absorption spectra discussed later will bring additional information on this point.

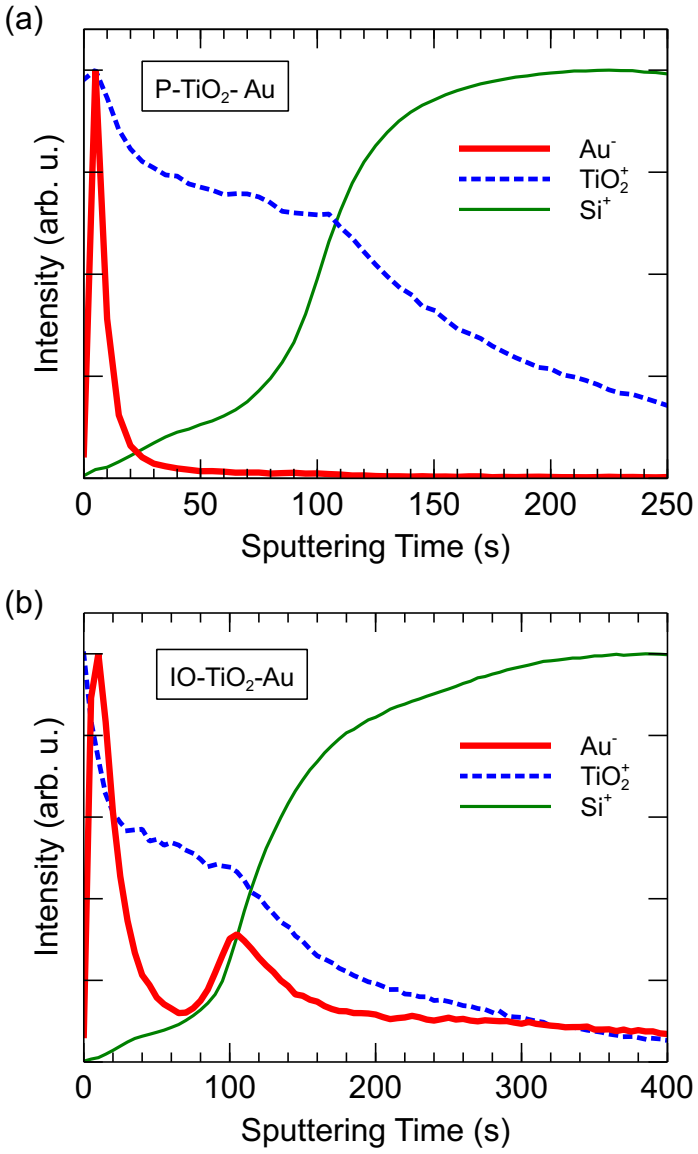

Figure 4: In-depth SIMS profiles of Au^- (197.0 u.m.a.), $TiO_2{}^+$ (79.9 u.m.a.) and Si^+ (28.01 u.m.a.) obtained for (a) P–TiO_2–Au and (b) IO–TiO_2–Au.

For the IO–TiO_2–Au inverse opal (Fig. 4b), the variation of the intensity of the Si^+ peak as a function of the sputtering time shows a step profile similar to P–TiO_2–Au.

The profile obtained for the TiO_2^+ peak shows a strong decrease in the first 20 s of sputtering, followed by a smoother decay up to around 110 s, and a faster decrease thereafter. This variation, together with the Si^+ profile, suggests that the deposit is removed after a sputtering time of about 110 s. The Au^- signal shows a strong peak in the first 30 s of sputtering, and then a weaker and broader peak at about 105 s. The first one corresponds to Au NPs deposited on the top layer of the spheres of the inverse opal structure. The second one is assigned to Au NPs deposited in the free spaces between the spheres (Figure 3), where the Si substrate is covered by a very thin film of TiO_2^+.

Planar films and inverse opals were studied by XPS to analyze the chemical state of the elements which constitute the synthesized samples. Figure 5 shows the spectra obtained for annealed P–TiO_2–Au and IO–TiO_2–Au samples in the spectral ranges corresponding to the Ti 2p, O 1s and Au 4f peaks.

The Ti 2p spectrum (Fig. 5a) shows for both samples the Ti $2p_{3/2}$ and Ti $2p_{1/2}$ peaks of Ti^{4+} at 458.80 eV and 464.50 eV, respectively, attesting that titanium is in the Ti^{4+} oxidation state [36]. This proves that the annealed samples are made of stoichiometric TiO_2.

The O 1s peak (Fig. 5b) shows for both samples a main component at 530.20 eV corresponding to Ti-O bonds in stoichiometric TiO_2 in agreement with the Ti 2p peak analysis [37]. A smaller component is observed at 531.80 eV. Its intensity is larger for IO–TiO_2–Au compared to P–TiO_2–Au. It is assigned to OH groups adsorbed on the surface of the samples [38].

This observation can be interpreted in two ways, which may be complementary. First, the higher relative intensity of the OH contribution may be due to the larger specific surface area of IO compared to planar films (at least 8 times larger), and thus a higher surface-to-bulk ratio analyzed by XPS. This leads to an increase of the relative intensity of the adsorbed species compared to the bulk species. Even if the whole surface is not hydroxylated, the contribution of OH species to the O 1s signal must be higher. On the other hand, Figures 3a and 3b show TiO_2 spheres composed of well differentiated particles that can present different crystallographic orientations. Very polar directions may appear, which require a larger hydroxylation than the most stable orientations to be stabilized. The larger specific surface area of inverse opals increases the contribution of adsorbed species such as hydroxyl groups. These two complementary effects can explain the higher contribution of the OH component in the O 1s spectrum of IO–TiO_2–Au.

The presence of Au at the surface of P–TiO_2–Au and IO–TiO_2–Au samples is shown in Figure 5a by the two Au 4f peaks near 84.0 eV ($4f_{7/2}$) and 87.7 eV ($4f_{5/2}$). These energy values are compatible with metallic gold without oxidation [39]. However, for the planar film, the asymmetry of the 4f peaks is not very marked, which can reflect a metallic character disturbed by the small size of the Au NPs. For the IO–TiO_2–Au sample, the Au 4f peak intensity is quite smaller due to the topography of the sample and the lower density of Au NPs deposited on the shells compared to the planar films (Fig. 3a), while a part of Au NPs is hidden under the TiO_2 spheres. Moreover, the spectrum shows a symmetric Au 4f peak which is slightly shifted towards higher binding energies (ca. 0.15 eV). These observations highlight the small size of the Au NPs which are perfectly dispersed on the surface of the TiO_2 shells.

Raman spectroscopy was used to check the structure of as-deposited and annealed

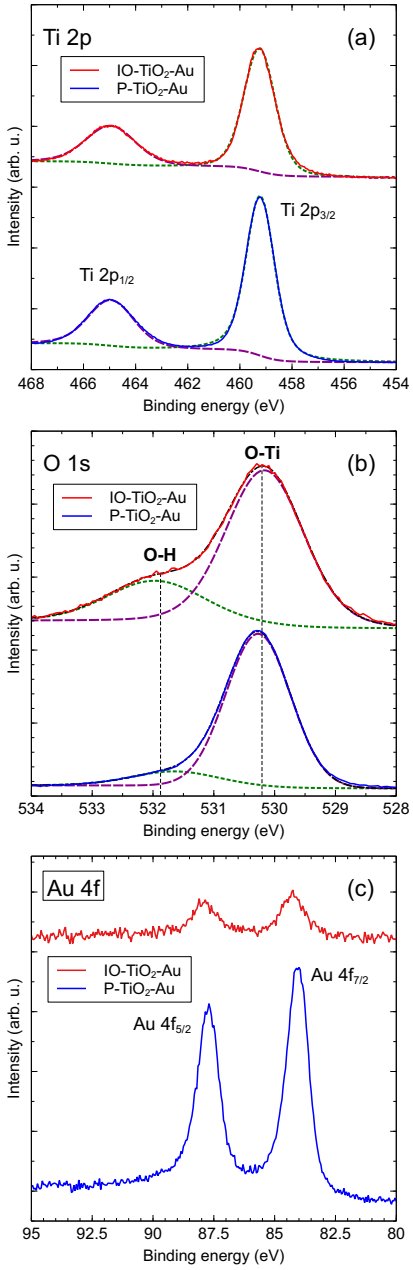

Figure 5: XPS spectra of P–TiO_2–Au (blue) and IO–TiO_2–Au (red). Spectral windows: (a) Ti 2p, (b) O 1s and (c) Au 4f.

TiO_2–Au films. The results presented in Figure 6 show only the Si peaks coming from the substrate for the as-deposited film. After annealing peaks are present at 145, 400 and 640 cm^{-1}. They are assigned to anatase TiO_2. Therefore, TiO_2 is amorphous in the as-deposited films and it crystallizes into the anatase structure during annealing at 380 °C. This is in agreement with previous works [33]. The spectrum obtained for TiO_2–Au inverse opals after the thermal treatment does not show any peak which can be assigned to the PS beads and in particular near the very strong peak at about 1000 cm^{-1}. Residues of the PS calcination give rise to the D and G bands assigned to amorphous carbon. The peaks of anatase TiO_2 are clearly detected at lower frequencies. In particular, the peak at 145 cm^{-1} is strong and the signal from the Si substrate is reduced in this case.

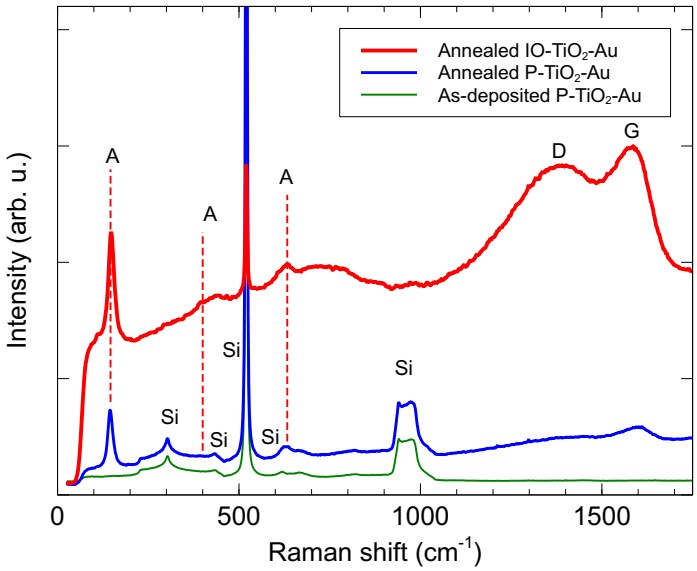

Figure 6: Raman spectra of P–TiO_2–Au and IO–TiO_2–Au after annealing at 380 °C. The spectra of as-deposited P–TiO_2–Au is shown for comparison.

3.2. Absorption tests and surface plasmon resonance

The optical absorption of P–TiO_2–Au planar films in the visible range was measured before studying their photocatalytic activity under visible light irradiation. A 90 nm thick film of TiO_2 was deposited on a quartz substrate by ALD. As described in section 2.1, Au-NPs were deposited next followed by a 10 nm thick TiO_2 film. A pure P–TiO_2 film deposited on a quartz substrate and the suspension of Au NPs diluted in ethanol used for the synthesis of composite samples were also studied for comparison. The results are shown in Figure 7.

As expected, no absorption bands are present in the visible range for the undoped P–TiO_2 film. The spectrum of the suspension shows an absorption band at about 520 nm which corresponds to the surface plasmon resonance of Au-NPs. This band

is redshifted in the P–TiO_2–Au spectrum which displays a broad absorption peak centered at about 580 nm.

The absorption cross-sections of spherical gold nanoparticles embedded in a medium of a given refractive index can be modeled using the Mie theory [40]. We used the optical constants for gold from [41]. For 5 nm diameter Au NPs in ethanol (n=1.36), the absorption band due to the surface plasmon resonance is calculated to be at 524 nm which is very close to the experimental position observed in Figure 7. For the same Au NPs embedded in anatase TiO_2 with a refractive index n=2.4, the surface plasmon resonance shifts to 631 nm. This redshift is significantly larger than the observed one for P–TiO_2–Au. This can be due to a partial coverage of gold NPs by TiO_2, but also to a refractive index lower than 2.4 if the TiO_2 deposit is porous. Indeed, only 10 nm of TiO_2 have been deposited on top of the Au-NPs. The experimental peak of P–TiO_2–Au near 580 nm is reproduced using a refractive index n=2.

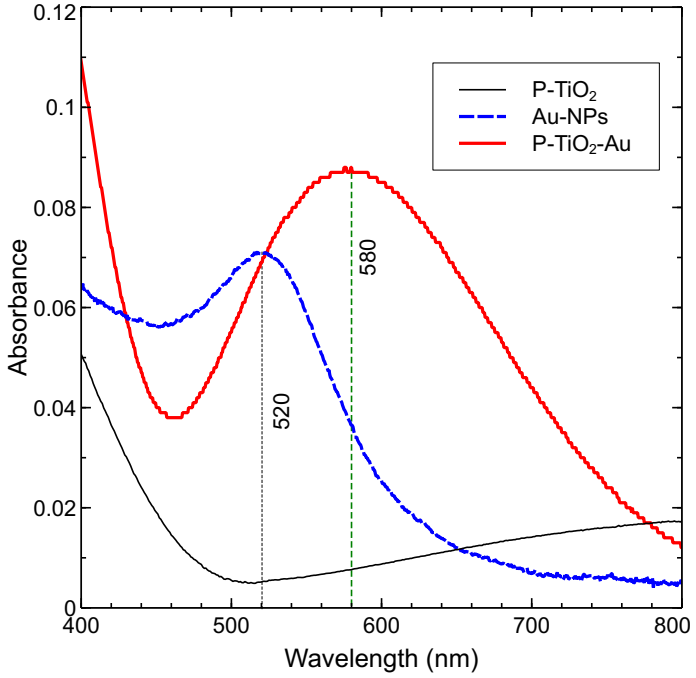

Figure 7: Absorption spectra in the visible range of a P–TiO_2 film (in black), a P–TiO_2–Au film (in red), both of them deposited on quartz substrates, and of the Au NPs suspension used for the synthesis of TiO_2–Au composite films (in blue).

3.3. Photocatalytic tests

3.3.1. Preliminary tests: natural degradation and pure TiO_2 photocatalyst

Before studying the efficiency of P–TiO_2–Au planar films and IO–TiO_2–Au inverse opals as photocatalysts for degrading methylene blue, the natural degradation of this

dye under visible light was studied as a function of time.

In the visible range, the aqueous solution of methylene blue has an intense and broad absorption band from about 550 to 700 nm, as shown in Figure 8 (black curve). The main component at about 664 nm corresponds to single MB molecules, while the second one at about 605 nm is assigned to dimers [42].

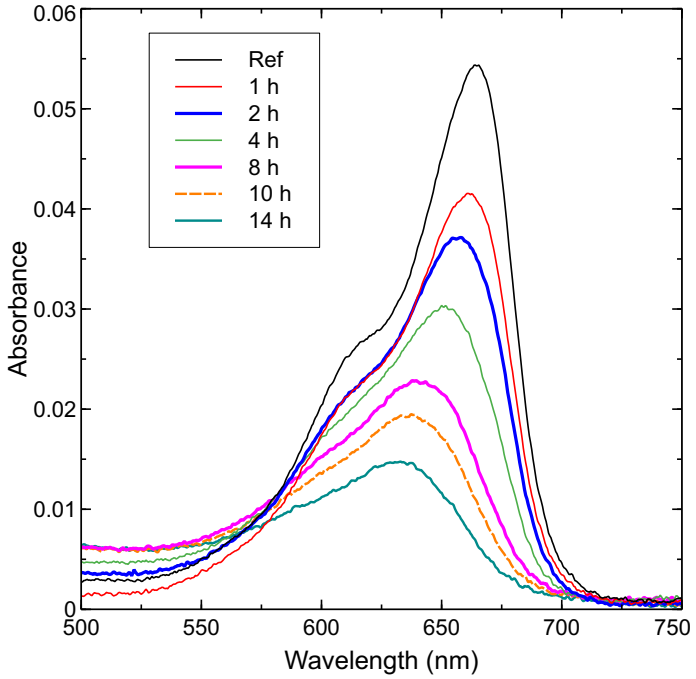

Figure 8: Time evolution of the absorption spectrum of a 1 μmol/L aqueous solution of methylene blue under visible-light irradiation without a photocatalyst (natural degradation).

Figure 8 shows the evolution of the absorption spectrum of 1 μmol/L concentrated aqueous solution of MB under visible-light. It shows a strong decrease of the absorption band, which is even faster for the main component at 664 nm. The natural degradation of MB occurs as a result of the absorption of a significant part of the spectrum of the lamp. The degradation of MB was assessed by the eq. 1 :

$$\text{Degradation } (\%) = (C_0 - C_t)/C_0 \cdot 100 \tag{1}$$

with C_t the concentration of the MB solution at time t, and C_0 the initial concentration.

The evolution of the natural degradation of MB under visible-light without any photocatalyst is shown in Figure 9a. The degradation reaches 23% after 1 h and 77% after 14 h. The variation with time was fitted with a first-order kinetics law (eq. 2):

$$\ln\left(\frac{C_0}{C_t}\right) = k \cdot t \tag{2}$$

where k is the apparent reaction constant and t the reaction time. The result is given in Figure 9b and confirms the first-order kinetics for the natural degradation of MB with an apparent reaction constant $k_{Nat.} = 0.100\ h^{-1}$. The aim of this work was to increase this degradation rate by using the synthesized photocatalysts.

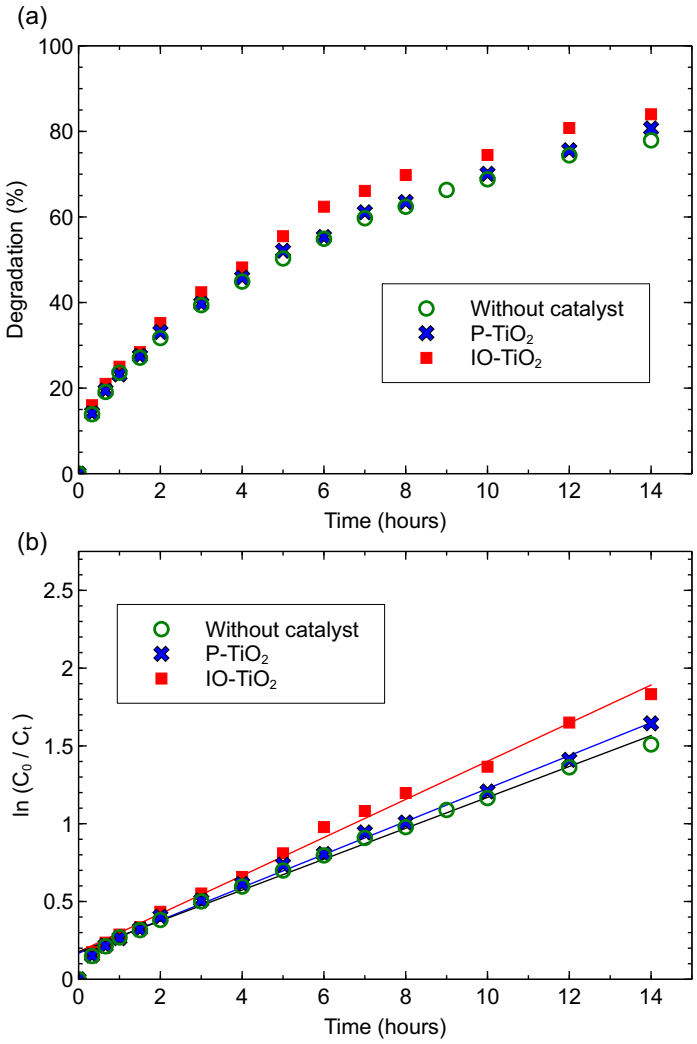

Figure 9: Degradation over time of a 1 μmol/L aqueous solution of methylene blue under visible-light irradiation using P–TiO_2 and IO–TiO_2 films as photocatalysts, compared to the natural degradation without a photocatalyst. (a) Degradation percentage, (b) degradation kinetics in logarithmic scale.

First, the degradation of MB by using P–TiO_2 and IO–TiO_2 as photocatalysts was studied under visible-light irradiation. A very small effect is expected because of the absence of absorption bands of TiO_2 in this range. The results are presented in Figure 9. The effect of the P–TiO_2 photocatalyst is almost negligible. The apparent reaction constant, $k_{P-TiO_2} = 0.106\ h^{-1}$, is very close to that of the natural degradation. For the IO–TiO_2 sample, a weak effect is observed with an apparent reaction constant $k_{IO-TiO_2} = 0.123\ h^{-1}$. This may be due to the larger specific surface area of the sample which provides many sites where MB molecules can adsorb and to the spectrum of the used lamp whose tail in the UV range may play a role.

3.3.2. Activity of TiO_2–Au composite photocatalysts

After the preliminary tests, the degradation of methylene blue was studied with the P–TiO_2–Au and IO–TiO_2–Au composite photocatalysts. The evolution of the degradation percentage over time is shown in Figure 10a. The two composite photocatalysts increased significantly the degradation rate of MB. The P–TiO_2–Au planar film allowed to obtain a 40% degradation for 2 h of exposure and more than 90% for 14 h, while the IO–TiO_2 photocatalyst induced a 95% degradation for only 7 h of exposure to visible-light illumination. These results are very encouraging compared to the literature [6]. They can certainly be improved in the future by increasing the density of gold nanoparticles and the synthesis of multilayer inverse opals.

The kinetics of MB degradation fits well to a first order law, as shown in Figure 10b. The values of the apparent reaction constant obtained for all the photocatalysts are summarized in Table 1. For P–TiO_2–Au, the apparent reaction constant is 0.157 h^{-1}, thus nearly 60% higher than natural degradation, while k=0.280 h^{-1} for the IO–TiO_2–Au inverse opal photocatalyst, thus 80% higher than natural degradation of MB. For comparison, the apparent reaction constant of MB degradation obtained using a IO-TiO_2 photocatalysts under ultraviolet light was k=0.240 h^{-1} [33]. The results obtained here under visible light are remarkable, and they show the coupling effect of TiO_2 to gold nanoparticles. As indicated in the Introduction section, the direct charge injection mechanism has been widely proposed in the literature to explain the higher photoactivity of TiO_2 nanostructures doped with noble metal nanoparticles [21, 23, 24]. The absorption of visible light that matches their plasmon resonance gives rise to e^-/h^+ charges in the noble metal nanoparticle. The direct charge injection mechanism is based on the transfer of these *hot* electrons from the nanoparticle to the conduction band of TiO_2 .

Houas et al. proposed a detail reaction pathway for the degradation of methylene blue in aqueous solutions using TiO_2 (Degussa P-25) as photocatalyst under UV illumination [43]. They argued that the photogenerated holes are not involved in the initial step of the degradation process since the reactant is cationic and not electron donor. It is the photogenerated electrons which, through the reduction of oxygen, give rise to the reactive oxygen species (ROS) involved in the initial phase of MB degradation. In the present case, under visible-light illumination, the hot electrons transferred to TiO_2 give rise to the ROS that trigger the MB degradation (Figure 11).

The synthesized composite TiO_2–Au inverse opal structure presents by far the best photocatalytic activity, leading to a degradation approximately three times faster than the natural degradation.

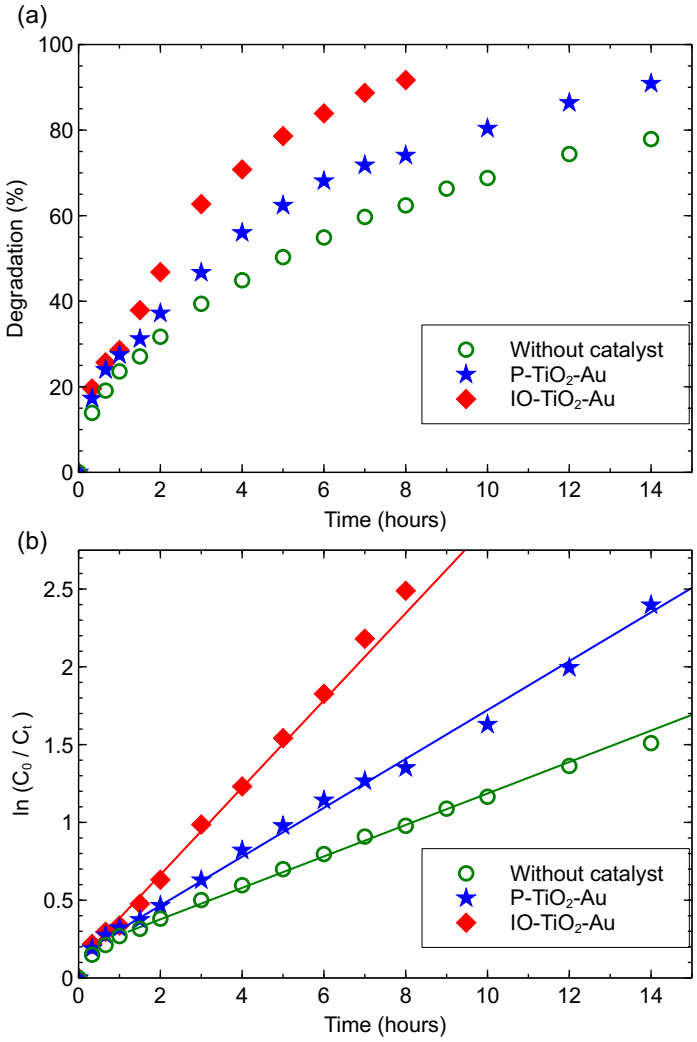

Figure 10: Degradation of methylene blue (1 μmol/L) over time under visible-light illumination using P–TiO_2–Au and IO–TiO_2–Au films as photocatalysts, compared to the natural degradation of MB. (a) Degradation percentage, (b) degradation kinetics in logarithmic scale.

4. Conclusions

TiO_2–Au composite planar films and inverse opals have been synthesized by Atomic Layer Deposition (ALD) using a Direct Liquid Injection (DLI) setup for TiO_2 deposition, and also for the injection of preformed Au nanoparticles (NPs). A few nanometers thick layer of TiO_2 was deposited by ALD after the Au NPs to increase the contact surface with the substrate and improve their adhesion to it. The annealing of the samples at 380 °C removed the template of polystyrene beads and led to crystallization of TiO_2

Photocatalyst	Apparent reaction constant, (h^{-1})
Natural degradation	$0.100\ (\pm 0.005)$
P–TiO_2	$0.106\ (\pm 0.005)$
IO–TiO_2	$0.123\ (\pm 0.005)$
P–TiO_2–Au	$0.157\ (\pm 0.005)$
IO–TiO_2–Au	$0.280\ (\pm 0.005)$

Table 1: Apparent reaction constants of the photocatalytic degradation of an aqueous solution of methylene blue (1 μmol/L) under visible-light irradiation for different photocatalysts compared to natural degradation.

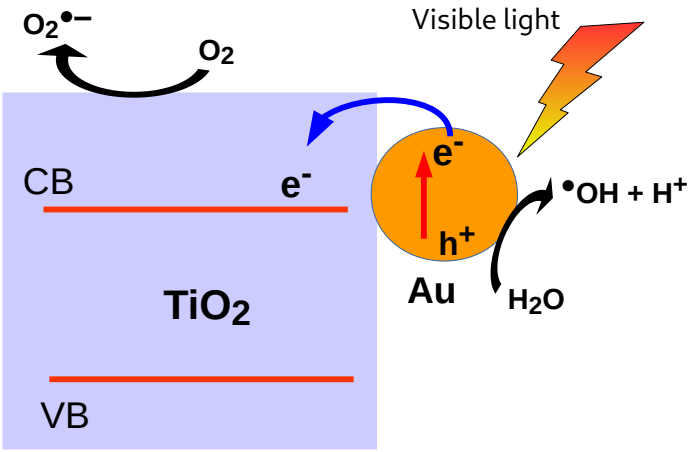

Figure 11: Direct charge injection mechanism in the coupling of TiO_2 to Au nanoparticles excited at the localized surface plasmon resonance.

in the anatase phase, as shown by Raman spectroscopy. The synthesis of stoichiometric TiO_2 was confirmed by XPS analysis, as well as the metallic state of gold.

SEM images of the synthesized inverse opals have shown their layered structure of hollow TiO_2 spheres interconnected by channels formed at the bead contact points in the templates, and the homogeneous distribution of Au NPs on the surface.

The absorption spectrum has shown the redshift of the localized surface plasmon resonance of the Au NPs from 520 nm for the suspension in ethanol to 587 nm in TiO_2–Au planar films. This suggests a partial coverage of gold NPs by the ultra-thin film of TiO_2 deposited, or the TiO_2 deposit is porous.

The degradation of methylene blue (MB) solutions was studied as a function of time to assess the photocatalytic activity of the synthesized composite structures under visible-light illumination. Pure–TiO_2 planar films and inverse opals were tested as photocatalysts, but the degradation of MB was similar to that observed for MB under visible illumination. The kinetics of MB degradation was fitted to a first order law.

For both TiO_2–Au planar films and inverse opals, the photocatalytic effect on MB degradation has been clearly observed. The P–TiO_2–Au planar film allowed to obtain

more than 90% for 4 hours of exposure to visible-light illumination, while the IO–TiO_2–Au photocatalyst induced a 95% degradation for only 7 h of exposure. The apparent reaction constant obtained for IO–TiO_2–Au photocatalyst was almost three times higher than that corresponding to natural degradation without photocatalyst. The higher photoactivity of TiO_2–Au planar films and inverse opals has been explained by the direct charge injection mechanism which is based on the transfer of *hot* electrons from the nanoparticle excited at its plasmon resonance to the conduction band of TiO_2. At the surface of TiO_2, they can give rise to reactive oxygen species involved in the initial stage of MB degradation.

All these results highlight the interest of composite TiO_2–Au inverse opals as photocatalysts for the degradation of dyes under visible-light irradiation. In addition, the potential of the ALD technique for the fabrication of complex composite structures using preformed nanoparticles has been shown.

Acknowledgments

This work is part of the project MPA 2017, supported by the Conseil Régional de Bourgogne Franche Comté through the plan d'actions régional pour l'innovation (PARI) and the European Union through the PO FEDER-FSE Bourgogne 2014/2020 programs.

P. B. acknowledges support from the French Ministry of National Education, Higher Education and Research, MENRT fellowship. This work has been supported by the EIPHI Graduate School (contract ANR-17-EURE-0002).

References

[1] F. Orts, A. I. del Río, J. Molina, J. Bonastre, F. Cases, Study of the reuse of industrial wastewater after electrochemical treatment of textile effluents without external addition of chloride, International Journal of Electrochemical Science (2019) 1733–1750 (2019). doi:10.20964/2019.02.27.

[2] D. A. Yaseen, M. Scholz, Textile dye wastewater characteristics and constituents of synthetic effluents: a critical review, International Journal of Environmental Science and Technology 16 (2019) 1193–1226 (2019). doi:10.1007/s13762-018-2130-z.

[3] M. Hazaraimi, P. Goh, W. Lau, A. Ismail, Z. Wu, M. Subramaniam, J. Lim, D. Kanakaraju, The state-of-the-art development of photocatalysts for the degradation of persistent herbicides in wastewater, Science of The Total Environment 843 (2022) 156975 (2022). doi:10.1016/j.scitotenv.2022.156975.

[4] R. B. González-González, R. Parra-Saldívar, W. F. Alsanie, H. M. Iqbal, Nanohybrid catalysts with porous structures for environmental remediation through photocatalytic degradation of emerging pollutants, Environmental Research 214 (2022) 113955 (2022). doi:10.1016/j.envres.2022.113955.

[5] U. Qumar, J. Zeb Hassan, R. Ahmad Bhatti, A. Raza, G. Nazir, W. Nabgan, M. Ikram, Photocatalysis vs adsorption by metal oxide nanoparticles, Journal of Materials Science and Technology 131 (2022) 122 – 166 (2022). doi:10.1016/j.jmst.2022.05.020.

[6] D. Chen, Y. Cheng, N. Zhou, P. Chen, Y. Wang, K. Li, S. Huo, P. Cheng, P. Peng, R. Zhang, L. Wang, H. Liu, Y. Liu, R. Ruan, Photocatalytic degradation of organic pollutants using TiO_2-based photocatalysts: A review, Journal of Cleaner Production 268 (2020) 0959 – 6526 (2020). doi:10.1016/j.jclepro.2020.121725.

[7] S. Yan, X. Ren, F. Zhang, K. Huang, X. Feng, P. Xing, Comparative study of Pb^{2+}, Ni^{2+}, and methylene blue adsorption on spherical waste solid-based geopolymer adsorbents enhanced with carbon nanotubes, Separation and Purification Technology 284 (2022) 120234 (2022). doi:10.1016/j.seppur.2021.120234.

[8] M. Mubarak, H. Selim, R. Elshypany, Hybrid magnetic core–shell TiO_2@$CoFe_3O_4$ composite towards visible light-driven photodegradation of methylene blue dye and the heavy metal adsorption: isotherm and kinetic study., Journal of Environmental Health Science and Engineering 20 (2022) 265–280 (2022). doi:10.1007/s40201-021-00774-y.

[9] I. Arora, H. Chawla, A. Chandra, S. Sagadevan, S. Garg, Advances in the strategies for enhancing the photocatalytic activity of TiO_2: Conversion from UV-light active to visible-light active photocatalyst, Inorganic Chemistry Communications 143 (2022) 109700 (2022). doi:10.1016/j.inoche.2022.109700.

[10] J. Arun, S. Nachiappan, G. Rangarajan, R. P. Alagappan, K. P. Gopinath, E. Lichtfouse, Synthesis and application of titanium dioxide photocatalysis for energy, decontamination and viral disinfection: a review, Environmental Chemistry Letters (2022). doi:10.1007/s10311-022-01503-z.

[11] L. Armelao, D. Barreca, G. Bottaro, A. Gasparotto, C. Maccato, C. Maragno, E. Tondello, U. L. Štangar, M. Bergant, D. Mahne, Photocatalytic and antibacterial activity of TiO_2 and Au/TiO_2 nanosystems, Nanotechnology 18 (2007) 375709 (2007). doi:10.1088/0957-4484/18/37/375709.

[12] C. G. Silva, R. Juárez, T. Marino, R. Molinari, H. García, Influence of excitation wavelength (UV or visible light) on the photocatalytic activity of titania containing gold nanoparticles for the generation of hydrogen or oxygen from water, Journal of the American Chemical Society 133 (3) (2011) 595–602 (2011). doi:10.1021/ja1086358.

[13] K. Nakata, T. Ochiai, T. Murakami, A. Fujishima, Photoenergy conversion with TiO_2 photocatalysis: New materials and recent applications, Electrochimica Acta 84 (2012) 103 – 111 (2012). doi:10.1016/j.electacta.2012.03.035.

[14] N. Serpone, A. V. Emeline, Semiconductor photocatalysis — past, present, and future outlook, The Journal of Physical Chemistry Letters 3 (2012) 673–677 (2012). doi:10.1021/jz300071j.

[15] S. W. Verbruggen, TiO_2 photocatalysis for the degradation of pollutants in gas phase: From morphological design to plasmonic enhancement, Journal of Photochemistry and Photobiology C: Photochemistry Reviews 24 (2015) 64 – 82 (2015). doi:10.1016/j.jphotochemrev.2015.07.001.

[16] H. Kiwaan, T. Atwee, E. Azab, A. El-Bindary, Photocatalytic degradation of organic dyes in the presence of nanostructured titanium dioxide, Journal of Molecular Structure 1200 (2020) 127115 (2020). doi:10.1016/j.molstruc.2019.127115.

[17] S. Shen, H. Li, J. jia Fu, H. B. Wang, Wastewater purification with different precursors of carbon dots dominated titanium dioxide: Mechanism insight, Journal of Alloys and Compounds 922 (2022) 166162 (2022). doi:10.1016/j.jallcom.2022.166162.

[18] N. T. Padmanabhan, N. Thomas, J. Louis, D. Treasa Mathew, P. Ganguly, H. John, S. C. Pillai, Graphene coupled TiO_2 photocatalysts for environmental applications: A review, Chemosphere 271 (2021) 129506 (2021). doi:10.1016/j.chemosphere.2020.129506.

[19] T. Liu, L. Li, X. Geng, C. Yang, X. Zhang, X. Lin, P. Lv, Y. Mu, S. Huang, Heterostructured MXene-derived oxides as superior photocatalysts for MB degradation, Journal of Alloys and Compounds 919 (2022) 165629 (2022). doi:10.1016/j.jallcom.2022.165629.

[20] H. Chakhtouna, H. Benzeid, N. Zari, A. el kacem Qaiss, R. Bouhfid, Recent progress on Ag/TiO_2 photocatalysts: photocatalytic and bactericidal behaviors, Environmental Science and Pollution Research 28 (2021) 44638–44666 (2021). doi:10.1007/s11356-021-14996-y.

[21] S. Linic, P. Christopher, D. B. Ingram, Plasmonic-metal nanostructures for efficient conversion of solar to chemical energy, Nature Materials 10 (2011) 911 (2011). doi:10.1038/nmat31517.

[22] X. Zheng, X. Yan, J. Ma, X. Yao, J. Zhang, L. Wang, Unidirectional/bidirectional electron transfer at the Au/TiO_2 interface operando tracked by sers spectra from Au and TiO_2, ACS Applied Materials and Interfaces 13 (2021) 16498 – 16506 (2021). doi:10.1021/acsami.1c02540.

[23] L. Lin, Q. Zhong, Y. Zheng, Y. Cheng, R. Qi, R. Huang, Size effect of Au nanoparticles in Au-TiO_{2-x} photocatalyst, Chemical Physics Letters 770 (2021) 138457 (2021). doi:10.1016/j.cplett.2021.138457.

[24] G. Žerjav, M. Roškarič, J. Zavašnik, J. Kovač, A. Pintar, Effect of Au loading on Schottky barrier height in TiO_2 + Au plasmonic photocatalysts, Applied Surface Science 579 (2022) 152196 (2022). doi:10.1016/j.apsusc.2021.152196.

[25] G. I. Waterhouse, M. R. Waterland, Opal and inverse opal photonic crystals: Fabrication and charac terization, Polyhedron 26 (2007) 356–368 (2007). doi:10.1016/j.poly.2006.06.024.

[26] J. Yu, J. Lei, L. Wang, J. Zhang, Y. Liu, TiO_2 inverse opal photonic crystals: Synthesis, modification, and applications - a review, Journal of Alloys and Compounds 769 (2018) 740 – 757 (2018). doi:10.1016/j.jallcom.2018.07.357.

[27] Y. Li, F. Piret, T. Léonard, B.-L. Su, Rutile TiO_2 inverse opal with photonic bandgap in the uv–visible range, Journal of Colloid and Interface Science 348 (2010) 43 – 48 (2010). doi:10.1016/j.jcis.2010.04.005.

[28] J. I. L. Chen, G. von Freymann, S. Y. Choi, V. Kitaev, G. A. Ozin, Amplified photochemistry with slow photons, Advanced Materials 18 (2006) 1915 – 1919 (2006). doi:10.1002/adma.200600588.

[29] Y. Zhao, B. Yang, J. Xu, Z. Fu, M. Wu, F. Li, Facile synthesis of Ag nanoparticles supported on TiO_2 inverse opal with enhanced visible-light photocatalytic activity, Thin Solid Films 520 (2012) 3515–3522 (2012). doi:10.1016/j.tsf.2011.12.076.

[30] F. Temerov, B. Ankudze, J. J. Saarinen, TiO_2 inverse opal structures with facile decoration of precious metal nanoparticles for enhanced photocatalytic activity, Materials Chemistry and Physics 242 (2020) 122471 (2020). doi:10.1016/j.matchemphys.2019.122471.

[31] A. Zulfiqar, F. Temerov, J. J. Saarinen, Multilayer TiO_2 inverse opal with gold nanoparticles for enhanced photocatalytic activity, ACS Omega 5 (2020) 11595–11604 (2020). doi:10.1021/acsomega.0c00833.

[32] Y. Wang, D.-B. Xiong, W. Zhang, H. Su, Q. Liu, J. Gu, S. Zhu, D. Zhang, Surface plasmon resonance of gold nanocrystals coupled with slow-photon-effect of biomorphic TiO_2 photonic crystals for enhanced photocatalysis under visible-light, Catalysis Today 274 (2016) 15–21 (2016). doi:10.1016/j.cattod.2016.01.052.

[33] P. Birnal, M. C. Marco de Lucas, I. Pochard, B. Domenichini, L. Imhoff, Photocatalytic properties of atomic layer deposited TiO_2 inverse opals and planar films for the degradation of dyes, Applied Surface Science 512 (2020) 145693 (2020). doi:10.1016/j.apsusc.2020.145693.

[34] L. Avril, S. Reymond-Laruinaz, J. Decams, S. Bruyère, V. Potin, M. C. Marco de Lucas, L. Imhoff, TiO_2 anatase films obtained by direct liquid injection atomic layer deposition at low temperature, Applied Surface Science 288 (2014) 201 – 207 (2014). doi:10.1016/j.apsusc.2013.10.007.

[35] L. Avril, S. Bourgeois, M. C. Marco de Lucas, B. Domenichini, P. Simon, F. Addou, J. Boudon, V. Potin, L. Imhoff, Thermal stability of Au–TiO_2 nanocomposite films prepared by direct liquid injection CVD, Vacuum 122 (2015) 314 – 320 (2015). doi:10.1016/j.vacuum.2015.06.018.

[36] A. R. Burke, C. R. Brown, W. C. Bowling, J. E. Glaub, D. Kapsch, C. M. Love, R. B. Whitaker, W. E. Moddeman, Ignition mechanism of the titanium–boron pyrotechnic mixture, Surface and Interface Analysis 11 (1988) 353–358 (1988). doi:10.1002/sia.740110614.

[37] M. Takagi-Kawai, M. Soma, T. Onishi, K. Tamaru, The adsorption and the reaction of NH_3 and NO_x on supported V_2O_5 catalysts: Effect of supporting materials, Canadian Journal of Chemistry 58 (2011) 2132–2137 (2011). doi:10.1139/v80-340.

[38] L. D. Setiawan, H. Baumann, D. Gribbin, Surface studies of keratin fibers and related model compounds using ESCA. I—intermediate oxidation products of the model compound 1-cystine and their hydrolytical behaviour, Surface and Interface Analysis 7 (1985) 188–195 (1985). doi:10.1002/sia.740070406.

[39] M. Casaletto, A. Longo, A. Martorana, A. Prestianni, A. Venezia, Xps study of supported gold catalysts: the role of Au^0 and Au^δ species as active sites, Surface and Interface Analysis 38 (2006) 215–218 (2006). doi:10.1002/sia.2180.

[40] L. Saviot, https://saviot.cnrs.fr/mie/index.en.html (2022). [link].
URL https://saviot.cnrs.fr/mie/index.en.html

[41] P. Johnson, R. Christy, Optical constants of the noble metals, Physical Review B 6 (1972) 4370–4379 (1972). doi:10.1103/PhysRevB.6.4370.

[42] N. Florence, H. Naorem, Dimerization of methylene blue in aqueous and mixed aqueous organic solvent: A spectroscopic study, Journal of Molecular Liquids 198 (2014) 255 – 258 (2014). doi:10.1016/j.molliq.2014.06.030.

[43] A. Houas, H. Lachheb, M. Ksibi, E. Elaloui, C. Guillard, J.-M. Herrmann, Photocatalytic degradation pathway of methylene blue in water, Applied Catalysis B: Environmental 31 (2001) 145 – 157 (2001). doi:10.1016/S0926-3373(00)00276-9.